JOURNAL OF PROPULSION AND POWER
Vol. 18, No. 3, May–June 2002

Solid-Fuel Regression Rate Behavior of Vortex Hybrid Rocket Engines

William H. Knuth,[*] Martin J. Chiaverini,[†] J. Arthur Sauer,[‡] and Daniel J. Gramer[§]
Orbital Technologies Corporation, Madison, Wisconsin 53717

A series of static engine firings were conducted to investigate the solid-fuel regression rate behavior and operating characteristics of vortex hybrid rocket engines. The vortex hybrid engine configuration is characterized by a coaxial, coswirling, counterflowing vortex combustion field in a cylindrical fuel port. To generate this flowfield, oxidizer is injected through a swirl injector located between the aft end of the fuel grain and the inlet to the converging portion of the exit nozzle. Test firings with thrusts up to 960 N were conducted with gaseous oxygen and hydroxyl-terminated polybutadiene solid fuel. Average fuel regression rates up to seven times larger than those in similar classical hybrids were measured. Empirical correlations were developed to describe accurately the experimental regression rates over more than an order of magnitude variation in mass flux. In addition to local mass flux and oxygen injection velocity, geometric engine variables, such as engine contraction ratio and length-to-diameter ratio, had a significant influence on the measured regression rates. Nondimensional regression rate and heat transfer correlations were also developed. Throttling and restart capability were demonstrated.

Nomenclature

A = cross-sectional area, cm^2
B = blowing parameter
c_p = isobaric specific heat, J/kg · K
D = port diameter, cm
E_a = activation energy, kcal/mole
G = local mass flux, kg/m^2 · s
G_{inj} = injection mass velocity, kg/m^2 · s
G_{O} = gaseous oxygen mass flux, kg/m^2 · s
h = enthalpy, J/kg
L = length, cm
M = momentum, kg · m/s^2
$\dot{m}$ = mass flow rate, kg/s
Nu = Nusselt number
Pr = Prandtl number, 0.7
p = pressure, psi
Q_c = convective heat flux, W/m^2
Re_D = Reynolds number based on port diameter
Ru = universal gas constant, kcal/mole · K
r = solid-fuel regression rate, mm/s
St = Stanton number
T = temperature, K
x = axial location from aft end of grain, cm
Y_i = mass fraction
ΔH_f° = heat of formation, J/kg, −124,300 for HTPB
ΔH_r = heat of reaction, J/kg
ΔH_v = heat of vaporization, J/kg
μ = gas viscosity, N · s/m^2, 6×10^{-5}
ρ_f = solid-fuel density, kg/m^3, 920

Subscripts

av = average
c = classical hybrid
inj = injector
O = oxidizer, reference
p = port
s = surface
sw = swirl
tan = tangent
tot = total

Introduction

HYBRID rockets have unique operational characteristics that can potentially provide safer, lower-cost avenues to space than current solid propellant and liquid bipropellant systems. Classical hybrid rocket engines can be throttled for thrust tailoring, perform in-flight motor shutdown and restart, and incorporate nondestructive mission abort modes. Also, because the fuel is stored in the form of a solid grain, classical hybrids require only half the feed system hardware of liquid bipropellant engines, providing a simpler, more flexible design with potentially improved reliability. The commonly used butadiene-based fuels are benign, nontoxic, and not hazardous to store and transport, unlike volatile liquid fuels such as hydrogen. Solid fuel grains are not highly susceptible to cracks, imperfections, and environmental temperature, as are solid propellant grains, and are, therefore, safer to manufacture, store, transport, and launch. Because of these safety and operational advantages, classical hybrid engines could display lower manufacture and launch costs than current propulsion systems.

Despite these benefits, classical hybrid rockets have not yet found widespread use for either commercial or military applications, possibly because they suffer from slow solid-fuel regression rates, low volumetric loading, and relatively poor combustion efficiency. Polymeric hybrid fuels, such as hydroxyl-terminated polybutadiene (HTPB), regress rather slowly, generally about an order of magnitude slower than solid propellants. To produce the necessary mass flow rate of pyrolyzed vapor from the fuel grain, consistent with a desired thrust level, complex grain cross-sectional geometries with large ports and wetted surface areas must be employed. Such grains require proportionally large pressure cases and display poor volumetric loading and high manufacturing cost. Recently, Casillas et al. have shown that a three- to fourfold increase in fuel regression

---

Presented as Paper 99-2318 at the AIAA/ASME/SAE/ASEE 35th Joint Propulsion Conference and Exhibit, Los Angeles, CA, 20–23 June 1999; received 10 November 2000; revision received 30 October 2001; accepted for publication 1 February 2002.

[*] Chief Engineer, Space Center, 1212 Fourier Drive. Associate Fellow AIAA.

[†] Lead Propulsion Engineer, Space Center, 1212 Fourier Drive. Member AIAA.

[‡] Aerospace Engineer, Space Center, 1212 Fourier Drive. Member AIAA.

[§] Lead Engineer, Space Center, 1212 Fourier Drive. Member AIAA.

rate can result in significant cost reductions, simplified grain manufacturing, and large reductions in inert weight.[1] Also note that low regression rates are also a disadvantage when small grain L/D ratios may be desirable, such as for upper stages.

The vortex hybrid engine is an alternative configuration to classical, head-end injected hybrids that has the potential to alleviate these problems and improve overall performance. The key characteristic of this engine is a unique coaxial, coswirling, counterflowing vortex pair that has been found to induce much higher solid-fuel regression rates than those of similar classical hybrid engines. To generate this flowfield, oxidizer, such as gaseous oxygen (GOX) is injected through a swirl injector located between the aft end of the fuel grain and the inlet to the converging portion of the exit nozzle. The injector ports are aligned circumferentially tangent, or nearly so, to the fuel grain surface. The outer vortex sweeps up along the fuel surface, mixing and burning with pyrolyzed fuel. At the engine head end, the outer vortex turns inward and transforms into an inner vortex that spirals downward toward the nozzle. The injected oxidizer is prevented from immediately flowing inward and out the nozzle by the strong radial pressure gradients and centrifugal forces associated with the tangential injection. This flow phenomenon is roughly analogous to the incompressible case of a volume of swirling water in a pail that is spinning fast enough to climb the cylindrical walls and leave a void across the central portion of the bottom of the pail. Even if the pail bottom contains a central hole, the water can be spun fast enough to prevent drainage.

Figure 1 shows a schematic diagram of an 89-N (20-lbf) thrust vortex hybrid engine (the VH-20), and a photograph of one of the hot firings. The gross features of the coaxial vortex flowfield are also shown schematically in Fig. 1a. Described more fully in the following section, the VH-20 had a transparent acrylic case for flow visualization. Both PMMA and HTPB fuel grains were tested in the engine. Figure 1b shows a PMMA fuel test where only the top 30% of the fuel grain was allowed to ignite, rendering visible the inner vortex in the center of the fuel grain. Figure 2 shows the axial velocity field calculated using the finite difference Navier–Stokes (FDNS) code during a companion computational fluid dynamics (CFD) effort to simulate vortex hybrid combustion under various conditions in a hypothetical 2100-kPa, 2225-N thrust engine burning GOX and HTPB. The FDNS flow solver utilizes a finite difference method for solving the nonlinear elliptic Navier–Stokes equations. The fuel port shown in Fig. 2 has a length and inner diameter of 23 and 13.4 cm, respectively. The GOX flow rate and velocity are 0.615 kg/s and 260 m/s, respectively. Reference 2 describes this work in detail and may be consulted for additional information. Here, it suffices to note that the numerical simulation confirmed qualitatively the coaxial vortex flowfield in the combustion chamber of a vortex hybrid engine. The outer vortex progresses along the fuel surface toward the engine head end, then forms an inner vortex that exits the nozzle, as shown in Fig. 2a. Figure 2b shows a close view of the injector region and converging portion of the exit nozzle. Notice that the inner vortex, in conjunction with the radial pressure gradient of the injected fluid and associated centrifugal forces, prevents the injected oxygen from immediately exiting the nozzle and instead causes it to flow toward the head end to join the inner vortex. Note that the minimum threshold injection momentum to produce the counterflowing vortex pair for a given port geometry has not been thoroughly investigated and represents an area of future research.

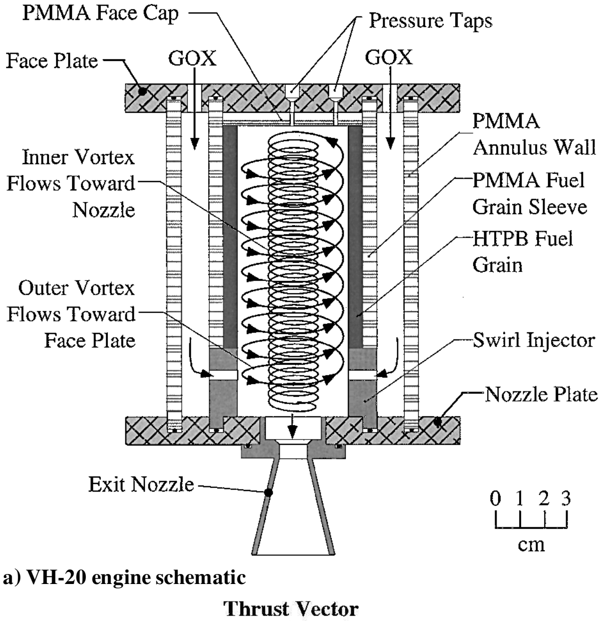

a) VH-20 engine schematic

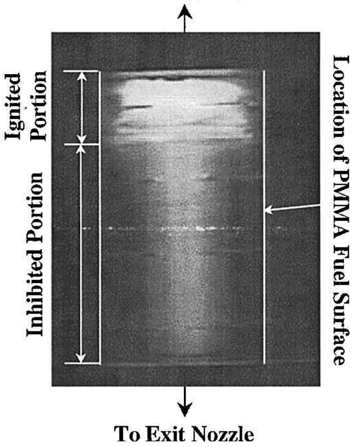

b) Hot-fire visualization test showing inner vortex

Fig. 1 Coaxial vortex flowfield in the VH-20 engine.

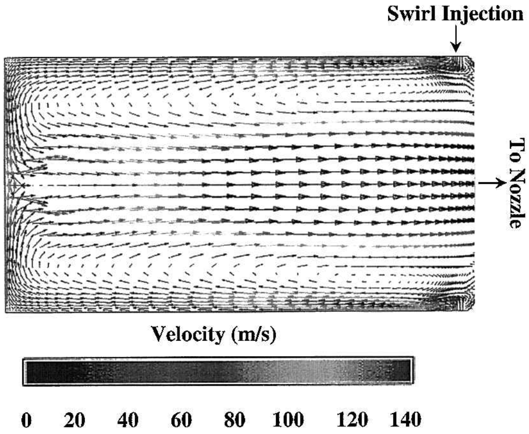

a) Combustion chamber

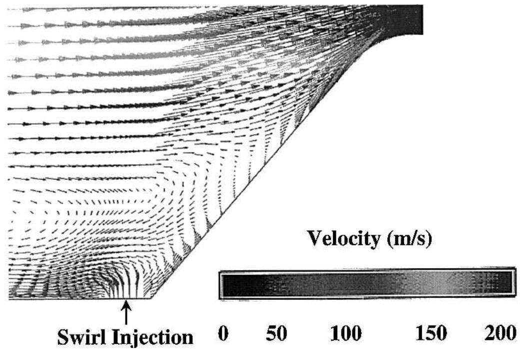

b) Close view of injector region and converging potion of exit nozzle

Fig. 2 Axial velocity field predicted by FDNS code for a 2225-N thrust vortex hybrid engine.

This paper describes the results obtained from an experimental test program to characterize the solid-fuel regression rate behavior of several vortex hybrid rocket engines of various sizes. The effort included a statistical test program conducted with a laboratory-scale engine, a second test program conducted with a larger engine, and the development of both engineering and scientific regression rate and heat transfer correlations. In addition to regression rate, the combustion efficiency represents another key parameter in hybrid rocket performance analysis. However, the highly swirling flowfield in the vortex hybrid has strong radial pressure gradients that complicate the use of a reference pressure for C^* calculations. In addition, the effect of swirl flow on the effective throat area and exit nozzle performance has not yet been thoroughly investigated, making impulse efficiency calculations difficult. Regression rate analysis, however, does not require a detailed characterization of the coaxial vortex flowfield. A future work will focus on characterizing the vortex flowfield, combustion behavior, and engine efficiency. As noted, Ref. 2 describes an initial numerical effort to investigate the coaxial vortex flowfield using a CFD approach.

Method of Approach

The experimental results were obtained from hot firings of both the VH-20 and a 445-N (100-lbf) thrust vortex hybrid engine (the VH-100). The VH-100 was later modified to operate at about 890 N (200 lbf) to further extend the range of test conditions. Figure 1 shows a schematic diagram of the VH-20 engine and HTPB fuel grain. The engine consists of a top injection plate, a bottom nozzle plate, a noncooled copper exit nozzle, and a cylindrical PMMA annulus wall. The flat top and bottom plates were square and constructed of aluminum. The PMMA wall had an outer diameter of 11.4 cm (4.5 in.) and a wall thickness of 6.4 mm (0.25 in.). The PMMA annulus wall and fuel grain were sandwiched between the two engine plates such that the grain was centered in the engine, as shown in Fig. 1. Tie bolts (not shown in Fig. 1) securely held the engine components together. The flexible engine design readily accommodated fuel grains of various lengths and diameters for the initial phase of testing.

GOX was injected into the annular space between the PMMA wall and fuel grain through two ports in the top engine plate. The pressure differential between the annulus and fuel grain then forced the GOX through the tangential injectors and into the combustion port. Pressure measurements were made at the oxygen annulus, at the center of the combustion port, and at a radial location 17.8 mm from the center of the combustion port. The annulus and combustion port pressure transducers were mounted to the top engine plate, as shown in Fig. 1.

HTPB fuel grains were cast and cured in acrylic tubes with inner and outer diameters of 6.4 and 7.6 cm, respectively. The head end of the HTPB fuel grains were capped with 0.64-cm-thick PMMA disks with ports to accommodate pressure measurements. Combustion port lengths ranged from 3.8 to 10.2 cm, and initial port inner diameters from 2.5 to 5.1 cm.

Figure 3 shows an assembly drawing of the VH-100 engine, comprising four main structural components: aluminum head dome, aluminum barrel, stainless steel nozzle clamp/lower manifold, and copper exit nozzle assembly. The barrel was 10.7 cm (4.2 in.) long and accommodated fuel cylinders 12 cm (4.75 in.) in outer diameter. The barrel wall thickness was 3.2 mm (0.125 in). The barrel and dome sections were bolted together using mating flanges. A second flange on the rear of the barrel was used for attaching the nozzle clamp. Several copper nozzle throat inserts with various throat diameters were used to provide partial control of chamber pressure. Most tests were conducted using 1.78-cm- (0.7-in.-) diam throats. For testing at higher oxygen flow rates and corresponding higher thrusts on the order of 890 N, a 2.24-cm (0.88-in.) throat diameter nozzle insert was used to prevent chamber pressures in excess of the 2400-kPa (350-psi) design pressure.

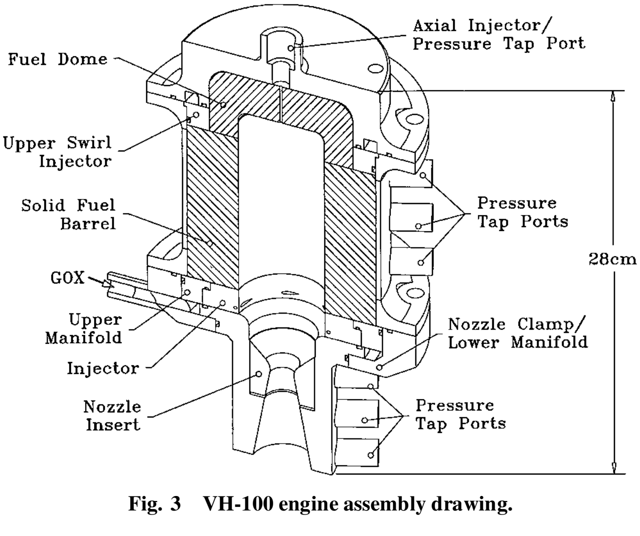

Fig. 3 VH-100 engine assembly drawing.

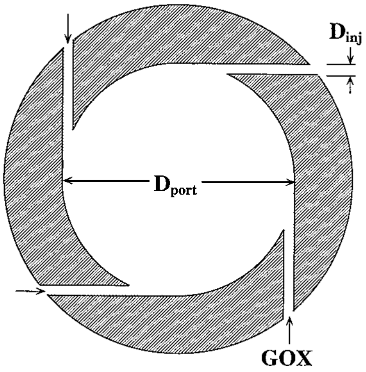

Fig. 4 Typical swirl injector.

The swirl injector was located at the rear of the engine between the bottom of the fuel cylinder and the entrance to the nozzle assembly, similar to the VH-20 engine. Figure 4 shows a cross-sectional view of a typical swirl injector, which is representative of that employed for both the VH-100 and VH-20 engines. The particular number and size of the injection ports varied for a given injector design.

The VH-100 engine was instrumented with 12 transducer ports at five radial stations across the head dome, three axial stations along the barrel, the lower GOX manifold, and three axial stations along the nozzle wall, including the throat and exit plane. Pressure ports were cast into the fuel grain barrels and domes to accommodate the transducers measurements. The radial pressure measurements through the fuel dome were made at 0, 0.89, 2.0, 3.15, and 4.3 cm from the engine axial centerline. The axial pressure measurements through the fuel barrel were made at 3.0, 6.1, and 9.2 cm from the base of the barrel. In addition, a 6675-N (1500-lbf) load cell sandwiched between the head end of the horizontally mounted engine, and a rigid thrust takeout structure was used to measure engine thrust. A pair of turnbuckle/spring assemblies were used to preload and stabilize the system. The chamber pressure transducer arrays were employed in an attempt to characterize the local radial pressure gradients in the combustion chamber. However, because pressure measurements had to be made directly through the fuel grain, one or more pressure ports often became clogged with soot during a given test, making consistent and accurate radial pressure measurements difficult.

The HTPB fuel grain barrels were 10.7 cm long and had initial inner and outer diameters of 5.1 and 12 cm, respectively. The barrels were cast in paper tubes (3.2 mm thick) for cartridge loading into the engine. The domes were cast separately and joined to the barrels during engine assembly using high-temperature silicone rubber sealant. Including the injector thickness, fuel barrel length, and fuel dome cavity, the initial engine port length was 14.6 cm (5.75 in.) for all tests reported here.

GOX flow to the engines was controlled using critical flow venturis and dome-loaded, computer-controlled pressure regulators. Engine throttling and restart was demonstrated by preprogramming the regulators to deliver a desired GOX flow rate profile during a given test. The GOX feed line was attached to the VH-100 engine lower manifold perpendicular to the thrust axis to minimize interference with the thrust measurements.

The HTPB fuel used for both the VH-20 and VH-100 test series was manufactured by curing R-45M homopolymer with a diisocyanate curing agent, Isonate 143L (Dow Chemical) in a mixture ratio of 100 parts R-45M to 11.37 parts Isonate 143L. To make the fuel opaque to thermal radiation, 0.5% by weight carbon black powder was added to the R-45M during the mixing process.

Ignition was achieved for both engines using a tuft of electrically heated steel wool inserted into the fuel grain center port through the exit nozzle. Rapid ignition was obtained when the steel wool was allowed to heat up for about 1.5 s before starting the oxygen flow.

Results and Discussion

Testing with the VH-20 engine was conducted to provide an initial characterization of vortex hybrid solid-fuel regression rate and combustion behavior and to assist in the development of the VH-100. An initial test series was performed to investigate grain ignition behavior and to begin refinement of the gross features of the tail-end swirl injection technique with the primary goal of achieving uniform regression rate along the port length. These early tests were successful, but are not described in detail here. Table 1 summarizes the VH-20 test series of current interest. This series consisted primarily of a two-level, 16-test screening matrix developed using statistical experimental design. The main objective of these tests was to determine which independent design variables had the greatest influence on average regression rate. Seven controllable test variables, each with two values, were employed and included GOX mass flow rate (0.016 and 0.028 kg/s), grain length (7.62 and 10.16 cm), initial grain port diameter (3.81 and 5.08 cm), exit nozzle diameter (1.14 and 1.4 cm), number of injection ports, total injection port area (sum of all injection port cross-sectional areas), and injection port upsweep angle with respect to the cross-sectional plane of the fuel grain. With this reference plane, an injection upsweep angle of 0 deg is perpendicular to the longitudinal axis of the fuel grain, whereas an angle of 90 deg is aligned with the longitudinal axis. A total of eight injectors were tested during the screening matrix test series. Each injector design had a unique combination of total injection area, number of injection ports, and injection port upsweep angle. Tests VH20-17 to -20 were conducted to provide additional data for correlation development. Incomplete ignition during Test VH20-20 caused the low average regression rate listed in Table 1. Burn times for the VH-20 test series were approximately 5 s. An error analysis indicated that the experimental error was about ±5% for the VH-20 test series.

Table 1 summarizes the average mixture ratio and regression rate results, obtained from fuel mass loss measurements. The average port diameter is also listed. The oxidizer mass flux G_O refers to the GOX mass flow rate into the engine divided by the average cross-sectional area of the combustion port:

$$G_O = \dot{m}_O / A_p \tag{1}$$

where A_p was calculated using D_{av}. Given the very different flowfields that occur between classical and vortex hybrids, the applicability of G_O as a physically significant operating condition for the latter case is somewhat open to discussion. However, G_O serves as a useful parameter for comparing classical and vortex hybrid regression rates under similar conditions. The local mass fluxes, including both fuel and oxidizer, listed in Table 1, correspond to those at an axial location of $x/L = 0.5$. These values were calculated using the average mixture ratio.

The injector mass velocity corresponds to the GOX mass flow rate divided by the total injection area (sum of all of the injection port cross-sectional areas):

$$G_{\text{inj}} = (\rho v)_{\text{inj}} = \dot{m}_O / A_{\text{inj}} \tag{2}$$

Note that the geometric area of the ports is used without any orifice loss correction terms.

The ratio of the regression rate obtained in the vortex motor to the regression rate that would occur in a classical hybrid operating at the same oxidizer mass flux is also shown in Table 1. The classical hybrid regression rate was calculated from[3]

$$r_c = 0.030\, G_O^{0.68} \tag{3}$$

where r_c is in millimeters per second and G_O in kilograms per meter squared seconds. Note from Table 1 that the VH-20 testing produced regression rates up to seven times larger than that of a similar classical hybrid.

Regression Rate Sensitivity Analysis

The time- and spatially averaged regression rates were determined from fuel grain weight loss measurements and analyzed using statistical methods. The axial uniformity of the regression rates were also evaluated for different injector designs. Space does not permit a full discussion of this analysis; however, Ref. 4 may be consulted for more details on the axial regression rate behavior.

Statistical design data analysis techniques were employed to determine the average regression rate's relative sensitivity to the test variables[5] using the data generated from the 16-firing screening test matrix shown in Table 1. Figure 5 shows the results of the statistical analysis, where all of the sensitivities are normalized with respect to the largest sensitivity. Negative sensitivities imply that the regression rate is inversely proportional to the variable, whereas positive sensitivities indicate a proportional relationship. Not surprisingly, the GOX mass flow rate into the combustion chamber has the largest effect on average regression rate. However, the initial grain port diameter also had a strong effect on the regression rate. This result

Table 1 Test matrix for VH-20 test series

Test no. VH20-	D_{av}, cm	Port length, cm	Exit nozzle diam, cm	Injector design	P_{ref}[a], kPa	O/F ratio	G_O, kg/m$^2\cdot$s	G, kg/m$^2\cdot$s	G_{inj}, kg/m$^2\cdot$s	r, mm/s	r/r_c
1	3.98	7.62	1.14	1	331.6	1.78	12.65	16.21	1061.2	0.57	3.33
2	5.37	7.62	1.40	2	77.9	1.42	7.45	10.07	1135.0	0.71	5.98
3	4.04	10.16	1.14	2	——	2.01	21.72	27.13	1875.5	0.76	3.09
4	5.38	10.16	1.40	1	505.9	1.33	12.14	16.68	1860.9	1.01	6.06
5	4.05	7.62	1.40	3	387.4	2.55	21.86	26.15	1245.0	0.79	3.18
6	5.38	7.62	1.14	4	753.4	1.66	12.62	16.41	1273.1	1.02	5.95
7	3.93	10.16	1.40	4	167.5	2.52	13.18	15.80	709.3	0.41	2.33
8	5.27	10.16	1.14	3	——	1.30	7.16	9.91	691.75	0.55	4.72
9	4.08	7.62	1.40	5	419.1	2.22	21.46	26.29	1887.5	0.89	3.62
10	5.44	7.62	1.14	6	847.1	1.45	12.24	16.46	1914.6	1.19	7.09
11	3.93	10.16	1.40	6	185.4	2.08	12.75	15.81	1040.4	0.39	2.27
12	5.30	10.16	1.14	5	389.5	1.15	7.41	10.64	1101.9	0.63	5.30
13	3.97	7.62	1.14	7	314.3	1.84	12.69	16.13	696.3	0.54	3.16
14	5.29	7.62	1.40	8	212.3	1.57	7.32	9.66	713.3	0.61	5.16
15	4.00	10.16	1.14	8	——	2.37	22.77	27.57	1266.3	0.63	2.47
16	5.32	10.16	1.40	7	477.7	1.63	13.00	16.98	1281.7	0.82	4.68
17	5.37	7.62	1.14	2	574.2	1.36	9.56	13.06	1459.1	0.97	6.84
18	5.39	7.62	1.14	2	672.1	1.50	11.17	14.89	1716.4	1.03	6.56
19	2.74	3.81	1.40	2	——	5.29	27.22	29.79	1080.7	0.66	2.30
20	2.60	3.81	1.40	2	——	21.52	54.06	55.31	1933.2	0.20	0.43

[a]Chamber pressure measured at a radius of 17.8 mm from engine centerline at head end. No measurements for tests 3, 8, and 15 due to soot clog in pressure port. Tests 19 and 20 had initial port radius smaller than pressure port at 17.8 mm.

Table 2 Test matrix for VH-100 test series

Test no. VH100-	GOX flow, kg/s	D_{av}, cm	$P_{\mathrm{ref}}{}^{\mathrm{b}}$, kPa	O/F	G_{O}, kg/m$^2\cdot$s	G, kg/m$^2\cdot$s	G_{inj}, kg/m$^2\cdot$s	Maximum thrust, N	r, mm/s	r/r_c
1–4[a]	0.05–0.07	——	——	——	——	——	——	——	——	——
5	0.116	6.01	1034	1.90	25.84	32.63	3244.9	311.5	1.44	5.18
6	0.114	5.77	1062	2.44	43.72	52.69	5061.6	311.5	1.81	4.55
7	0.114	5.57	1517	2.96	46.68	54.58	5030.9	311.5	1.87	4.49
8	0.146	5.95	1530	2.36	52.43	63.55	6464.2	427.2	2.30	5.10
9	0.145	5.96	1840	2.43	52.07	62.79	6423.4	471.7	2.30	5.14
10	0.147	5.61	1282	4.59	59.45	65.93	6513.2	351.6	1.40	2.85
11	0.148	7.20	1496	2.56	36.36	43.45	6555.5	427.2	1.78	5.08
12	0.161	6.09	1675	3.49	55.18	63.08	7108.2	445.0	1.70	3.65
13	0.092	6.48	1048	2.20	27.88	34.21	4077.4	258.1	1.41	4.82
14	0.148	6.48	1744	2.22	44.84	54.93	6551.4	480.6	2.20	5.42
15	0.091	6.05	1020	2.30	27.14	33.04	3453.4	231.4	1.23	4.26
16	0.165	5.91	1785	2.49	60.13	72.20	7296.6	502.9	2.36	4.78
17	0.091	5.38	903	2.67	39.98	47.45	4025.8	195.8	1.58	4.23
18	0.117	5.65	1234	3.11	46.54	54.03	5158.7	307.1	1.55	3.73
19	0.140	5.72	1420	2.84	54.23	63.77	6176.5	356.0	1.81	3.92
20	0.114	6.76	1137	2.36	27.68	33.54	4395.4	284.8	1.34	4.60
21	0.162	5.42	1916	1.79	70.22	89.88	7162.1	413.9	3.60	6.55
22	0.34	5.96	1861	3.86	121.8	137.6	6825.9	956.8	3.0	3.8
23	0.35	6.21	1799	4.92	115.6	127.4	6228.4	890.0	2.5	3.3

[a] System checkout runs using the same fuel grain. Detailed measurements not taken.

[b] Chamber pressure measurements correspond to maximum steady pressure at particular radii that vary for each test.

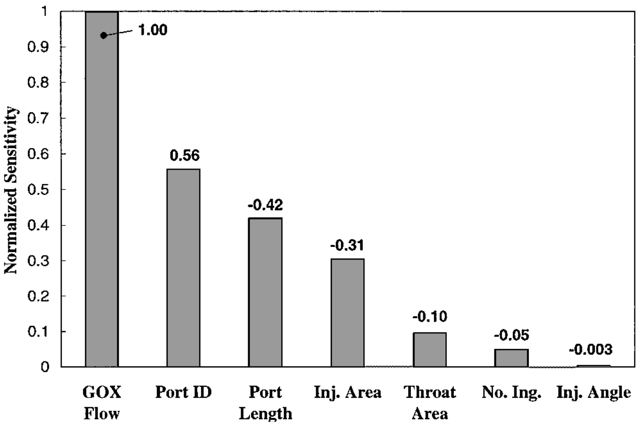

Fig. 5 Sensitivity of average regression rate to the independent test variables.

implies that, all other things being equal, higher regression rates result at relatively large port i.d. for the range of operating conditions and grain designs considered here.

On the other hand, the average regression rates decreased with increasing grain port length and larger total injection orifice areas. The reciprocal dependence on injection area suggests that fuel regression benefits from relatively high jet velocities issuing from the injection ports, which should help to form stronger coaxial vortices in the engine. The decrease in average regression rate with increasing port length may be caused by several mechanisms, including tangential momentum losses along the fuel port due to viscous interactions. In addition, local, postfiring fuel web thickness measurements indicated relatively high regression rates immediately downstream from the swirl injector, probably due to coherent oxygen jets enhancing fuel regression in this region.[5] This effect has a relatively larger impact on the average regression rate for shorter fuel grains, leading to the negative sensitivity to port length. In Ref. 5 these findings are discussed in greater detail.

The nozzle exit throat area, number of injection ports, and upsweep angle of the injector all had relatively small and negative effects on the average regression rate. Smaller throat areas lead to larger engine contraction ratios, which may accommodate the formation of more coherent coaxial vortex pairs by reducing the relative effect of viscous losses on vortex strength. Similar results were found using the CFD analysis, as described in Ref. 2. For a given total injection port area, fewer injection ports may enhance regression slightly by providing stronger jets that propagate further along the combustion chamber than would a larger number of weaker (smaller) jets. Larger injection ports also cause relatively smaller boundary-layer effects on the oxidizer jets. Finally, it appears that the spiraling rate of the outer vortex is determined by the chamber geometry and injection velocity, and not by the geometric angle of the injection ports, leading to the small sensitivity to injector upsweep angle.

Based on the sensitivity analysis results, injector design 2 was chosen for tests 17–20 because it offered the best combination of injector port area (small), number of injection ports (small), and injection port upsweep angle (small).

Regression Rate Correlations with Operating Conditions

Based on the initial internal ballistic characterization provided by the VH-20 test series, the VH-100 test series was conducted to extend the range of operating conditions examined during the investigation and to obtain a broader experimental database for regression rate correlation development. Table 2 summarizes the operating conditions and regression rates of these test firings. The oxidizer and local mass fluxes were based on the average port diameter. The injection mass velocity was calculated using Eq. (2). The average regression rates were determined from fuel mass loss measurements. Tests 22 and 23 constitute the 890-N (200-lbf) class tests, identified in later plots as VH-200 data. A 2.24-cm nozzle throat was used for both of these tests. Burn times for the VH-100/200 test series were between 5 and 10 s, depending on the particular test objective. Error analysis indicated that the experimental error was about ±5% for the VH-100/200 test series.

Figure 6 illustrates the relationship among G_{O}, port diameter, L/D ratio, and regression rate for the VH-20 and VH-100/200 test series. The classical hybrid regression rate, corresponding to Eq. (3), is also shown. At the same oxidizer mass flux level, the VH-20 data display widely different regression rates because of port geometry effects. Consistent with the sensitivity analysis, larger port diameters and smaller L/D ratios benefit higher regression rates, with port diameter having the stronger effect. For the same L/D ratio of 2, the 5.1-cm port grains had significantly higher regression rates, by about 60%, than the 3.8-cm port grains. Different injector designs cause most of the interfamily scatter among the groups of data. However, there is little difference between injector designs 2 and 6. At the largest initial port diameter of 5.1 cm and the smallest L/D ratio of 1.5, the vortex hybrid has an average regression rate about seven times larger than that of a similar classical hybrid. The VH-100/200 data correspond to testing with an injector very similar

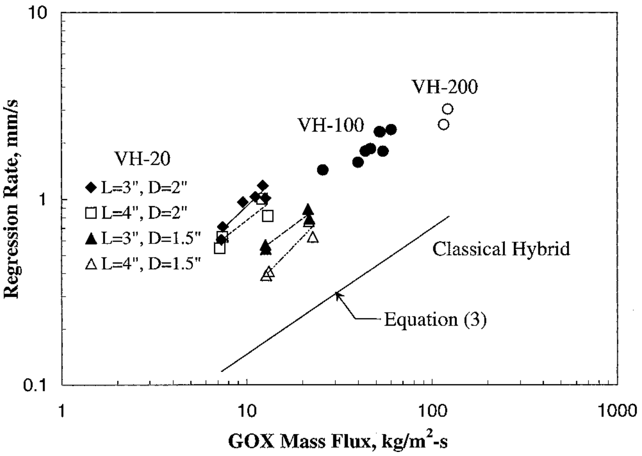

Fig. 6 Average regression rate behavior.

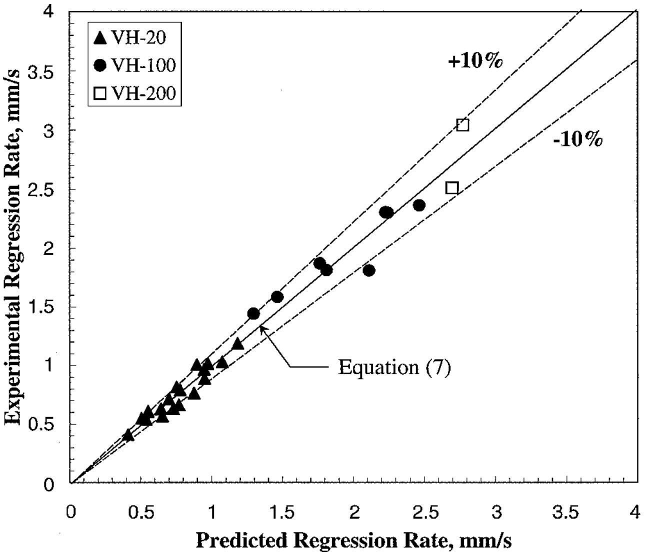

Fig. 7 Regression rate correlation with operating conditions.

to that of injector design 2 of the VH-20 test series. The system checkout tests (tests VH100-1 to VH100-4) are not included on the plot because detailed regression rate measurements were not made. Tests VH100-13 and VH100-18 did not yield reportable data, whereas tests VH100-10 to VH100-12 were conducted to assess an alternative injector design and are likewise not included in Fig. 6 or subsequent data analysis.

Empirical correlations were developed to describe the average regression rates of the VH-20 and VH-100/200, a function of operating conditions. As indicated by the sensitivity analysis, it was found that engine geometry played an important role in predicting the experimental regression rates. A least-squares fitting procedure using a statistical analysis code yielded

$$r = 0.0085\mathrm{CR}^{0.45}(L/D)^{-0.59}G_{\mathrm{inj}}^{0.45}G^{0.37}, \qquad R^2 = 0.977 \tag{4}$$

where the engine contraction ratio (CR) is defined as the ratio of the average port diameter to the throat diameter:

$$\mathrm{CR} = D_{\mathrm{av}}/D_t \tag{5}$$

In Eq. (4), r is in millimeters per second and the mass flux terms are in kilograms per meter squared seconds. Figure 7 shows the results of the correlation given by Eq. (4) as applied to the experimental regression rates. Equation (4) predicts the data from the VH-20 tests and the VH-100/200 tests series to a reasonable accuracy. Most of the data fit within a ±10% error band.

Equation (4) shows that, like classical hybrids, the regression rate depends on the port mass flux because higher mass fluxes cause larger convective heat fluxes to drive solid-fuel regression. However, higher injection mass fluxes also cause larger regression rates by increasing the vortex swirl velocity.[2] Therefore, the port mass flux plays a somewhat reduced role in the correlation. Note that the summation of the powers on the mass flux terms equals 0.82, similar to the theoretical 0.8 dependence predicted for the regression rate behavior of classical hybrids.

The reciprocal relationship between regression rate and L/D ratio probably results from several effects, including vortex strength dissipation along the fuel port due to viscous interactions in the flowfield. Engines with relatively large L/D would probably inhibit uniform coaxial vortex formation along the fuel port because viscous interactions and jet momentum dissipation could limit the propagation distance of the outer vortex along the fuel wall. The CFD analysis reported in Ref. 2 predicted decreasing vortex strength with increasing L/D ratio (Fig. 4 or Ref. 3). For larger L/D, a stronger vortex is required to reach the head end effectively and form the downward-spiraling inner vortex.[2]

The importance of the engine contraction ratio in the regression rate correlation is also consistent with the qualitative results of the CFD analysis.[2] Reference 2 shows that larger contraction ratios allowed stronger, more uniform coaxial vortices to develop in the combustion chamber. Smaller contraction ratios cause the outer vortex to be highly compressed against the fuel surface, creating an adverse environment for the coaxial vortex formation and causing more rapid swirl velocity dissipation.[2] These results also agree with the sensitivity analysis, which suggested that short chamber length, large chamber diameter, and small exit nozzle area all benefited higher, more uniform regression rates.

It is encouraging that a single expression represents the data reasonably well over more than an order of magnitude variation in port mass flux, injection mass velocity, and engine thrust. In addition, no explicit scaling effects were required to correlate the experimental regression rates, CR and L/D seem to contain the necessary variables to describe the effects of engine geometry, at least for the engines sizes considered here.

Finally, note that the engine chamber pressure did not represent an important variable for correlating the experimental regression rates. For classical hybrid engines, thermal radiation and gas-phase chemical kinetic processes have sometimes been shown to cause a pressure sensitivity in empirical regression rates correlations. However, the solid-fuel regression rate behavior in the vortex hybrid engine is dominated by high convective heat transfer rates driven by the coaxial vortex flowfield.

Nondimensional Regression Rate and Heat Transfer Correlations

Equation (4) represents a useful engineering correlation for use in designing vortex hybrid engines and predicting average regression rates as a function of design geometric variables and controllable operating conditions. However, the formulation of an analytical regression rate model is important for obtaining a more thorough understanding of the physical processes that govern the solid-fuel regression behavior in vortex hybrid engines.

The model of solid-fuel regression developed during the 1960s by Marxman and Gilbert[6] for classical hybrids serves as a useful starting point for the analysis of the vortex hybrid engine. By considering an energy flux balance on the fuel surface, for convective heat transfer, Marxman and Gilbert showed that[6]

$$\rho_f r/G = 0.023Re_D^{-0.2}Pr^{-0.7}(St/St_0)B \tag{6}$$

The Stanton number ratio in Eq. (6) accounts for the reduction in convective heat flux to the fuel caused by the blowing action of the vapor entering the boundary layer from the surface. As shown by Marxman et al.,[7] it is possible to obtain an empirical expression for the Stanton number ratio in terms of B, thus simplifying Eq. (6).

For the vortex hybrid engine configuration, additional analysis is required to explain the influence of swirling flow on the regression process. For heat transfer in tubes subject to swirling flow from a tangential injector, but in the absence of wall blowing and combustion, Dhir and Chang[8] found experimentally that

$$\frac{Nu_{\mathrm{sw}}}{Nu_{\mathrm{O}}} = 1 + 1.93\left(\frac{M_{\tan}}{M_{\mathrm{tot}}}\right)^{0.6} Pr^{-\frac{1}{7}} \exp\left[-m\left(\frac{x}{D_h}\right)^{0.6}\right] \tag{7}$$

where

$$m = 0.89(M_{\tan}/M_{\mathrm{tot}})^{0.2} Re_D^{-0.18} Pr^{-0.083} \tag{8}$$

and the tangential-to-total momentum ratio in Eq. (8) can be calculated using

$$\frac{M_{\tan}}{M_{\mathrm{tot}}} = \frac{\dot{m}_{\tan}^2}{\dot{m}_{\mathrm{tot}}^2}\frac{\rho A_p}{\rho A_{\mathrm{inj}}} \tag{9}$$

The momentum ratio and the mass flow rate ratio used in Eq. (9) correspond to those calculated at the outlet of the injector, where the flow rate of oxygen is well known. Because the local flow properties were not measured, the local momentum ratio can not readily be determined. From simple trigonometry,

$$\dot{m}_{\tan} = \dot{m}_{\mathrm{tot}} \cdot \cos(\theta) \tag{10}$$

Equation (9) can now be rearranged using Eq. (10) and the definitions of G_{O} and G_{inj} to obtain

$$M_{\tan}/M_{\mathrm{tot}} = \cos^2(\theta)(G_{\mathrm{inj}}/G_{\mathrm{O}}) \tag{11}$$

where the density ratio in Eq. (9) is unity.

Because $Nu = St\, Re\, Pr$, the left side of Eq. (7) can be rewritten as

$$Nu_{\mathrm{sw}}/Nu_{\mathrm{O}} = St_{\mathrm{sw}}/St_{\mathrm{O}} \tag{12}$$

The term $St_{\mathrm{sw}}/St_{\mathrm{O}}$ accounts for the enhanced local heat transfer due to tangential injection. Defining the Stanton number for the vortex hybrid as St_v, one can write

$$St_v = St_{\mathrm{O}}(St_{\mathrm{sw}}/St_{\mathrm{O}})(St_v/St_{\mathrm{sw}}) \tag{13}$$

The ratio of St_v to St_{sw} accounts for the additional effects of wall blowing, combustion, and the presence of the inner vortex field that are not considered in Dhir and Chang's[8] swirling pipe flow analysis. When St is replaced by St_v, Eq. (6) can now be rearranged using Eq. (13) to yield

$$\rho_f r/G = 0.023 Re_D^{-0.2} Pr^{-0.7}(St_{\mathrm{sw}}/St_{\mathrm{O}})(St_v/St_{\mathrm{sw}})B \tag{14}$$

In Eq. (14), the first Stanton number ratio is given by Eqs. (7–12), and accounts for enhanced heat transfer from swirling flow, whereas the second ratio accounts for the changes in heat transfer behavior that accompany the unique case of vortex hybrid combustion.

A computer code was developed to assist in calculating the various terms in Eq. (14). Energy and mass flux balances were used to determine the convective heat flux incident on the fuel surface[9]:

$$Q_c = \rho_f r\left(\sum_i^n Y_i \Delta H_{f,i}^{\mathrm{O}} - \Delta H_{f,\mathrm{HTPB}}^{\mathrm{O}} + \sum_i^n Y_i \int_{T\,\mathrm{ref}}^{Ts} c_{p,i}\, \mathrm{d}T\right) \tag{15}$$

Equation (15) was derived assuming the species diffusion velocities leaving the fuel surface and the kinetic energy terms associated with fuel regression and vaporization were negligible.[9]

The fuel surface temperature T_s was calculated by using an Arrhenius law to describe the solid-fuel regression rate as a function of surface temperature, namely,

$$r = A\exp(-E_a/R_u T_s) \tag{16}$$

Reference 10 shows that for pure HTPB, $E_a = 4.91$ kcal/mole and $A = 11.04$ mm/s for surface temperatures greater than 722 K and $E_a = 13.35$ kcal/mole and $A = 3{,}965$ mm/s for surface temperatures less than 722 K. Because the regression rates are known experimentally, Eq. (16) can be rearranged and solved for the surface temperature:

$$T_s = E_a/R_u \ln(A/r) \tag{17}$$

which, in turn, can be used in Eq. (15) to calculate Q_c. The mass fractions of the pyrolyzed species Y_i, and their respective heats of formation, were also taken from Ref. 10. These data were obtained from a gas-chromatograph/mass spectrometer with rapid-heating pyrolysis oven. Polynomial expressions for the individual species' isobaric specific heats $c_{p,i}$ were taken from Ref. 11 and used in the integral term of Eq. (10). Additional constants used in the analysis are listed in the Nomenclature.

With the convective heat flux calculated to a reasonable approximation from Eq. (15), the Stanton number can be found using[6]

$$St = Q_c/G(\Delta H_r - h_{\mathrm{wall}}) \tag{18}$$

where the heat of reaction of HTPB/GOX, ΔH_r, has been used to replace the enthalpy at the flame, h_{fl}, assuming an adiabatic combustion process. The heat of reaction for the combustion of GOX and HTPB at particular chamber pressures and mixture ratios was calculated using a chemical equilibrium code.[12] The reference Stanton number for turbulent pipe flow was calculated using[13]

$$St_{\mathrm{O}} = 0.023 Re_D^{-0.2} Pr^{-0.7} \tag{19}$$

where the Reynolds number was calculated based on the average port diameter.

The blowing number B was calculated using

$$B = \frac{\Delta H_r - h_{\mathrm{wall}}}{[\Delta H_v + c_s(T_s - T_{\mathrm{ref}})]} \tag{20}$$

which may be interpreted as the ratio of the thermal energy of the main stream relative to the surface to the thermal energy required to pyrolyze a unit mass of solid fuel. Smoot and Price[14] and Green[15] give similar definitions for B. Note that Marxman et al.[7] defined the Stanton number in terms of G at the flame, leading to an alternate definition of B. For the present analysis, G corresponds to the average mass flux across the fuel port at $x/L = 0.5$.

In Eqs. (18) and (20), h_{wall} and ΔH_v, were found from

$$h_{\mathrm{wall}} = \left(\sum_i^n Y_i \int_{T\,\mathrm{ref}}^{Ts} c_{p,i}\, \mathrm{d}T\right) \tag{21}$$

$$\Delta H_v = \sum_i^n Y_i \Delta H_{f,i}^{\mathrm{O}} - \Delta H_{f,\mathrm{HTPB}}^{\mathrm{O}} \tag{22}$$

The results of this analysis were used to obtain semi-empirical regression rate and heat transfer correlations for both the VH-20 and VH-100/200 data. An expression was first developed to describe the behavior of the regression rate with respect to the dimensionless groups shown in Eq. (14). However, the statistical analysis program was allowed to vary the preconstant [0.023 in Eq. (14)]. A least-squares analysis provided the following correlation for a combination of the VH-20 and VH-100/200 engine data:

$$\rho_f r/G = 0.023 Re_D^{-0.2}(St_{\mathrm{sw}}/St_{\mathrm{O}})(St_v/St_{\mathrm{sw}})B, \qquad R^2 = 0.938 \tag{23}$$

where $Pr = 0.7$ was absorbed into the preconstant. Note that the classical value of 0.023 for the constant gave the best fit to the data. However, this correlation caused a discrete clumping of the two data sets representing the VH-20 and VH-100/200 firings, suggesting that, although Eq. (23) is fairly accurate, it does not properly represent the regression rate behavior over the full range of Reynolds numbers.

A more accurate correlation was developed by allowing both the power on the Reynolds number and the preconstant in Eq. (9) to vary. The results of this analysis yielded

$$\rho_f r/G = 0.082 Re_D^{-0.33}(St_{\mathrm{sw}}/St_{\mathrm{O}})(St_v/St_{\mathrm{sw}})B, \qquad R^2 = 0.992 \tag{24}$$

The significantly higher R^2 value of 0.992 indicates the improved accuracy of this correlation. Equation (24) also has improved accuracy over the dimensional correlation of Eq. (4) even though only two free parameters (0.082 and −0.33) were used to fit the data. Figure 8 displays the results of Eq. (24) as applied to the experimental data.

It is encouraging that the experimental regression rates agree to a reasonable extent with the theoretical model developed here. This result suggests that the vortex hybrid regression rates were dominated by convective heat transfer processes, on which the theoretical expression given by Eq. (14) is based. However, the power of −0.33 on the Reynolds number does indicate that the boundary-layer processes in the vortex hybrid engine differ from those in conventional pipe flow, as might be expected. The reaction zone in the hybrid boundary layer may cause the shape of the velocity profile to differ from that of ordinary turbulent flow, which could lead to the particular Reynolds number dependency indicated by Eq. (24). Also note that the regression rates depends strongly on the characteristics of the coaxial vortex flow field. This influence enters into Eq. (19) through the St_{sw}/St_O term, which is a function of the tangential-to-total fluid momentum ratio M_{tan}/M_{tot}.

Mathematical relationships between the Stanton number ratios and the blowing parameter were also developed and are shown in Fig. 9. As expected, the data show a reciprocal relationship between B and St_v/St_O. An increase in B represents an increase in wall blowing caused by fuel vaporization. Because wall blowing tends to block some of the heat transfer from the gas phase to the fuel surface, larger values of B correspond to lower Stanton number ratios and vice versa. However, the magnitude of St_v/St_O is quite large compared to conventional hybrids due to the high heat fluxes induced by the coaxial vortex flowfield. At smaller blowing numbers, the values of St_v/St_O are about 30, whereas at larger blowing numbers the St_v/St_O values are about 4. In contrast, classical hybrids generally have been shown to have Stanton number ratios of less than unity due to the blocking effect of fuel vaporization on heat transfer to the fuel surface. Although this effect is also present in the vortex hybrid engines, the highly swirling flow causes much larger heat transfer rates to the fuel surface in comparison to classical hybrids.

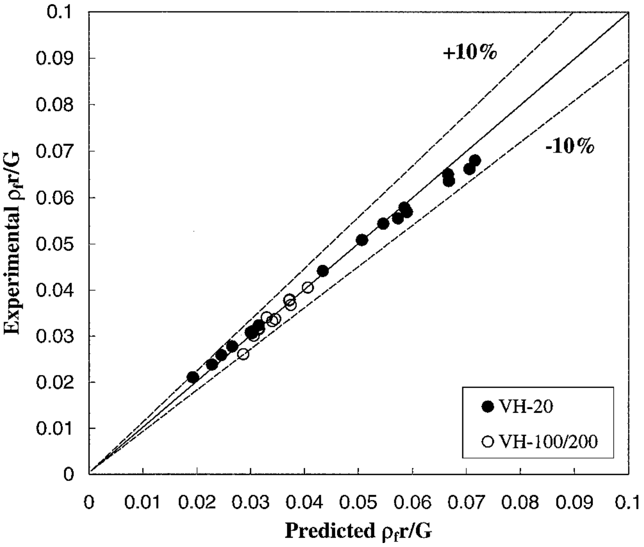

Fig. 8 Semi-empirical regression rate correlation.

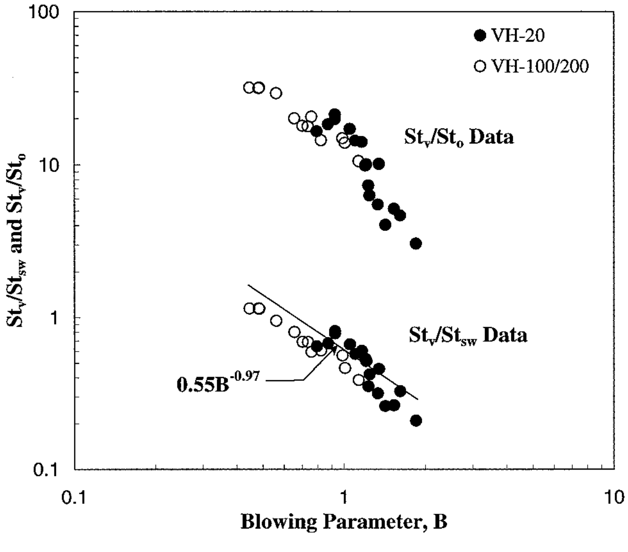

Fig. 9 Stanton number ratio behavior.

It is also instructive to compare the vortex hybrid Stanton numbers to those calculated for a reference swirling flow in a tube with no combustion or wall blowing. Figure 9 also shows the behavior of St_v/St_{sw} with respect to B. Although these data also show a reciprocal relationship between St_v/St_{sw} and B, the values of the Stanton number ratio lie below unity in almost all cases, indicating that wall blowing reduces the heat transfer as compared to the reference swirl flow case. However, at the smallest blowing numbers, St_v/St_{sw} exceeds unity by about 15%. This result suggests that the shear effects in the boundary layer differs somewhat due to the presence of the diffusion flame. As also indicated by the power of −0.33 on the Reynolds number in Eq. (24), the flame zone may alter the velocity profile, allowing the vortex hybrid to sometimes display larger heat transfer rates than the reference swirling flow, even in the presence of wall blowing. In their numerical investigation, Merkle and Venkateswaran[16] found that the diffusion flame zone caused a steeper velocity gradient near the fuel surface than would normally occur for noncombusting turbulent flow. Chiaverini et al.[17] also found evidence of this effect in experimental regression rate data obtained in a large lab-scale hybrid engine, where the Stanton numbers calculated for the hybrid engine sometimes exceeded the reference Stanton number (for noncombusting turbulent flow in a pipe).

A least-squares fit to the data in Fig. 9 indicated that

$$St_v/St_{sw} = 0.55B^{-0.97}, \qquad R^2 = 0.868 \tag{25}$$

Thus, the ratio of vortex hybrid to reference swirling flow Stanton numbers decreases approximately linearly with respect to B. This dependence on the blowing parameter is somewhat larger than that calculated by Marxman et al. for classical hybrids, where St/St_O was found to vary with B to the −0.77 power.[7] Substituting Eq. (25) into Eq. (24) shows that the vortex hybrid regression rates are approximately independent of B, at least for the range of blowing parameters tested here. However, because the R^2 value in Eq. (24) is significantly larger than that provided by Eq. (25), combining these two equations would degrade the accuracy of the regression rate correlation [Eq. (24)].

Throttling and Restart Tests

Practical hybrid engine operation may include thrust modulation via oxidizer throttling and restart capability. Tests VH100-14, VH100-15, and VH100-20 were conducted to investigate vortex hybrid performance for restart, throttling, and a combination of throttling/restart, respectively. For test VH100-14, the fuel was ignited and allowed to burn for 4 s, after which time the oxygen valve was closed. The thrust and engine pressures then began to drop as combustion ceased. After a shutoff time of 1.5 s, the engine was restarted by opening the oxygen run valve. The burn time for the second portion of the test was 2.5 s. The oxygen flow rate was 0.148 kg/s (0.326 lbm/s) for both segments of the test. Reignition was achieved by simply flowing oxygen into the combustion chamber by opening the run valve. It appears that the fuel surface remained hot enough during the shutdown interval to reestablish combustion. No other ignition source was required. The pressure and thrust traces rise rapidly back to their earlier levels after restart, indicating a rapid ignition. In addition, no pressure oscillations were measured,

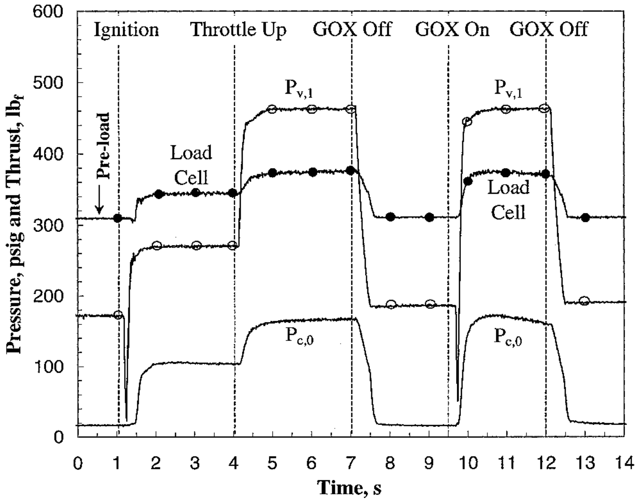

Fig. 10 Pressure and thrust profiles for a throttling and restart test.

indicating stable combustion. The engine achieved a thrust level of about 445 N (100 lbf) for both segments of test 14. The overall solid-fuel regression rate and O/F ratio were 2.2 mm/s and 2.22, respectively.

For test VH100-15, the initial GOX flow rate was 0.09 kg/s. The fuel was ignited and burned continuously until shutdown 8 s later. After 3 s at the initial flow rate, however, the GOX flow rate was throttled back to 0.06 kg/s for 3 s. During this segment of the test, the engine produced about 134 N of thrust. After 6 s, the GOX flow rate was increased to the initial level of 0.09 kg/s. During this interval, the engine thrust was about 223 N. The thrust and chamber pressures respond relatively quickly to changes in the oxygen flow rate, achieving quasi-steady levels within a few tenths of a second of the flow rate change. A portion of this delay is due to the finite response time of the GOX feed system with respect to an input from the control program. The average solid-fuel regression rate and O/F ratio for test 15 were 1.2 mm/s and 2.3, respectively. Again, the engine demonstrated stable combustion.

Throttling and restart were both performed during test VH100-20. Figure 10 shows the corresponding thrust and pressure profiles. The plot labeled $P_{v,1}$ shows the variation in GOX line pressure just upstream of the critical flow venturi and indicates the modulation of the GOX mass flow rate into the engine. The plot labeled $P_{c,0}$ shows the corresponding combustion chamber pressure variation at the center of the head end. A preload of approximately 1380 N (310 lbf) was applied to the thrust takeout system to prevent mechanical jitter and is indicated on the load cell profile. The initial GOX flow rate and thrust were 0.07 kg/s and 180 N (40 lbf), respectively. The combustion time at this flow rate was approximately 2.5 s. The GOX flow rate was then increased to 0.12 kg/s (0.26 lbm/s), corresponding to a thrust of about 310 N (70 lbf). After a 3-s burn at this higher flow rate, the oxygen run valve was closed. Ignition was achieved after a shut down time of 2.5 s by restarting the GOX flow at 0.12 kg/s. Again, the hot fuel surface provided an adequate ignition source. As in tests 14 and 15, the chamber pressures and thrust respond well to changes in the oxygen flow rate. The average solid-fuel regression rate and O/F ratio for test 20 were 1.34 mm/s and 2.36, respectively. As in all earlier tests, no significant pressure oscillations were measured.

Summary

Vortex hybrid rocket engines are characterized by a unique coaxial flowfield generated using swirl injection of oxidizer at the aft end of the fuel grain. An experimental investigation was conducted to characterize the solid-fuel regression rate behavior of such engines burning GOX and HTPB. A laboratory-scale engine in the 89-N thrust range was used to conduct a statistical test program to identify operating conditions that had a significant effect on average solid-fuel regression rate. A second test series was conducted in a larger engine in the 445–890 lbf range. A regression rate correlation based on design conditions was developed to describe both sets of data. A semi-empirical method was also employed to assist in developing physically descriptive dimensionless regression rate and heat transfer correlations. Engine throttling and restart were demonstrated as well.

Average solid-fuel regression rates up to seven times faster than those in similar classical hybrids were measured in the vortex hybrid engines. However, an upper bound on regression rate enhancement was not established. It is theorized that the high-velocity, swirling gas near the fuel surface induced high convective heat fluxes, which sustained the large regression rates. In addition, fuel surface attack by oxidizer from the injected jets may also contribute to regression rate enhancement under some conditions, especially in the aft-end region of the fuel grain. Reasonably uniform regression rate profiles along the length of the grain port were obtained with proper swirl injector design. Statistical analysis and empirical correlations indicated that the port geometry in the vortex hybrid had a very significant effect on the regression rate, with relatively wide, short ports favoring higher regression rates. The injector mass velocity also had a strongly positive effect on the regression rates, whereas the port mass flux was found to play a less important role than in conventional hybrid engines. An accurate correlation for regression rate data was developed using the contraction ratio, the port L/D ratio, the injection mass velocity, and the local mass flux. No explicit scaling factors were necessary to correlate the data accurately.

The theoretical regression rate analysis provided a sound basis for describing the experimental regression rate behavior in terms of dimensionless heat transfer parameters. It was found that the dimensionless fuel mass flux $(\rho_f r/G)$ correlated well with Reynolds number, the blowing parameter, and two Stanton number ratios. This two-parameter correlation proved slightly more accurate than the engineering correlation based on design variables. An examination of the Stanton number ratios showed that heat transfer rates in the vortex hybrid were generally much higher than those of classical hybrids, but lower than those of swirling flow in pipes due to the blocking action of fuel pyrolysis on heat flux to the fuel surface. In addition, the dimensionless correlations suggest that the boundary-layer processes in the vortex hybrid engine differ from those in conventional pipe flow. Alteration of the local velocity profile by the turbulent reaction zone represents a possible explanation for this behavior. Also note that heterogeneous surface reactions may contribute to the deduced Stanton number magnitude and behavior under some conditions.

The test program demonstrated successful throttling and restart of the vortex hybrid engine. The engine pressure and thrust profiles responded quickly to variations in the oxygen mass flow rate without introducing combustion instability.

It is believed that the results of this investigation will provide a strong foundation for continuing investigations of vortex hybrid flowfield analysis, regression rate behavior, performance characteristics, and larger-scale engine development for practical applications.

Acknowledgments

This Phase II Small Business Innovation Research effort was funded by NASA Marshall Space Flight Center (MSFC) under Contract NAS8-97015. The authors sincerely thank B. Shackleford, Contract Officer's Technical Representative, for his encouragement and support. The assistance of C. Martin, NASA/MSFC, in test matrix planning and data analysis is very highly appreciated. Additional thanks go to the U.S. Army for the use of their facilities at the Badger Army Ammunition Plant.

References

[1] Casillas, E. D., Shaeffer, C. W., and Trowbridge, J. C., "Cost and Performance Payoffs Inherent in Increased Fuel Regression Rates," AIAA Paper 97-3081, July 1997.

[2] Knuth, W. H., Chiaverini, M. J., Gramer, D. J., Sauer, J. A., St. Clair, C. P., Whitesides, R. H., and Dill, R. A., "Preliminary Computational Fluid Dynamics Analysis of the Vortex Hybrid Rocket Chamber and Nozzle Flowfield," AIAA 98-3351, July 1998.

[3] Sutton, G., *Rocket Propulsion Elements: An Introduction to the Engineering of Rockets*, 6th ed., Wiley, New York, 1992, p. 513.

[4] Knuth, W. H., Chiaverini, M. J., Gramer, D. J., and Sauer, J. A., "Experimental Investigation of a Vortex-Driven High-Regression Rate Hybrid Rocket Engine," AIAA 98-3348, July 1998.

[5] Box, E. P., George, H., William, G., and Hunter, J. S., *Statistics for Experimenters*, Wiley, New York, 1978, pp. 306–509.

[6] Marxman, G. A., and Gilbert, M., "Turbulent Boundary Layer Combustion in the Hybrid Rocket," *Ninth International Symposium on Combustion*, Academic, New York, 1963, pp. 371–383.

[7] Marxman, G. A., Wooldridge, C. E., and Muzzy, R. J., "Fundamentals of Hybrid Boundary Layer Combustion," *Heterogeneous Combustion*, edited by H. G. Wolfhard, I. Glassman, and L. Green, Jr., Vol. 15, Progress in Astronautics and Aeronautics, Academic, New York, 1964, pp. 485–521.

[8] Dhir, V. K., and Chang, F., "Heat Transfer Enhancement Using Tangential Injection," *ASHRAE Transactions: Symposia*, Vol. 98, Pt. 2, 1992, pp. 383–390.

[9] Chiaverini, M. J., *Regression Rate and Pyrolysis Behavior of HTPB-Based Solid Fuels in a Hybrid Rocket Motor*, Ph.D. Dissertation, Dept. of Mechanical Engineering, Pennsylvania State Univ., University Park, PA, Dec. 1997.

[10] Chiaverini, M. J., Harting, G. C., Lu, Y. C., Kuo, K. K., Peretz, A., Jones, S., Wygle, B., and Arves, J. P., "Pyrolysis Behavior of Hybrid Rocket Solid Fuels Under Rapid Heating Conditions," *Journal of Propulsion and Power*, Vol. 15, No. 6, 1999, pp. 888–895.

[11] Reid, R. C., Prausnitz, J. M., and Poling, B. E., *The Properties of Gases and Liquids*, McGraw–Hill, New York, 1987, p. 657.

[12] McBride, B. J., and Gordon, S., *Computer Program for Calculation of Complex Chemical Equilibrium Compositions and Applications*, NASA Reference Publication 1311, NASA John H. Glenn Research Center at Lewis Field, Cleveland, OH, June, 1996, pp. 143–146.

[13] Incropera, F. P., and DeWitt, D. P., *Fundamentals of Heat and Mass Transfer*, 3rd ed., Wiley, New York, 1990, p. 496.

[14] Smoot, L. D., and Price, C. F., "Regression Rates of Metalized Hybrid Fuel Systems," *AIAA Journal*, Vol. 4, No. 5, 1966, pp. 910–915.

[15] Green, L., "Introductory Considerations on Hybrid Rocket Combustion," *Heterogeneous Combustion*, edited by H. G. Wolfhard, I. Glassman, and L. Green, Jr., Vol. 15, Progress in Astronautics and Aeronautics, Academic, New York, 1964, pp. 451–484.

[16] Venkateswaran, S., and Merkle, C. L., "Size Scale-Up in Hybrid Rocket Motors," AIAA Paper 96-0647, Jan. 1996.

[17] Chiaverini, M. J., Kuo, K. K., Peretz, A., and Harting, G. C., "Regression Rate and Heat Transfer Correlations for Hybrid Rocket Combustion," *Journal of Propulsion and Power*, Vol. 17, No. 1, 2001, pp. 99–110.